

ARTICLE OPEN

Near-infrared absorption of π -stacking columns composed of trioxotriangulene neutral radicalsYasuhiro Ikabata¹, Qi Wang^{2,3}, Takeshi Yoshikawa¹, Akira Ueda^{4,5}, Tsuyoshi Murata^{3,4,6}, Kazuki Kariyazono⁴, Miki Moriguchi⁴, Hiroshi Okamoto⁷, Yasushi Morita^{3,4,6} and Hiromi Nakai^{1,2,3,8}

A long-wavelength photoabsorption of organic molecules has been noticed because of the potential as materials. In addition to the extension of π conjugation, molecular aggregation has been utilized to realize the elongation of absorption wavelength. We report strong near-infrared absorptions of trioxotriangulene neutral radicals in the crystalline state and large-scale theoretical calculations of the radical assemblies interpreting the mechanism of optical properties. Polarized absorption spectra and X-ray diffraction of the crystals clarified that an unusual π -stacking column consisting of π -dimers is key for this absorption. Quantum chemical calculations based on time-dependent density functional theory revealed that the π -dimer shows an electronic transition between frontier orbitals generated by strong coupling of the delocalized singly occupied orbitals of monomers. The interdimer interaction of transition dipole moments, which are parallel to the column, elucidated the increase of absorption wavelength. The divide-and-conquer Green function method enabled the large-scale time-dependent density functional theory calculation up to a 60mer, where the maximum number of atoms is 4380, reproducing the near-infrared absorptions of trioxotriangulene crystals. The present method to investigate the mechanism of the long-wavelength photoabsorption is useful for developing organic materials consisting of stable neutral radicals.

npj Quantum Materials (2017)2:27; doi:10.1038/s41535-017-0033-8

INTRODUCTION

π -Conjugated molecules absorbing near-infrared (NIR) light have been noticed in the researches of various applications.^{1, 2} One of the methodologies to design a molecule showing low-energy absorption involves the extension of π -conjugated systems that narrow the highest occupied molecular orbital (HOMO)-lowest unoccupied molecular orbital (LUMO) gap. In two extreme examples, the absorption band of zinc(II) porphyrin (400 nm) exhibits a red-shift in the fused tape-shaped array (3500 nm, dodecamer),^{3, 4} and the giant hydrocarbon sheet, C₂₂₂H₄₂, shows a broad absorption band around 250–1400 nm.⁵ π -Stacking also increases the absorption wavelength, since the intermolecular overlap of π -orbitals causes exciton delocalization. This kind of low-energy absorption can also be utilized for materials such as organic solar cells made from the *J*-aggregate of lead phthalocyanine.⁶ The π -stacked arrays of open-shell molecules are known to exhibit further lower energy absorption with large absorbance. One-dimensional (1D) columns of ion-radical species of tetracyanoquinodimethane and tetrathiafulvalene derivatives exhibit NIR absorption bands at 1000–2000 nm.^{7–10}

1D π -stacked arrays of neutral π -radicals, which we term ' π -stacked radical polymers',¹¹ are constructed without formation of the σ -bonds, and absorb long-wavelength light. Phenalenyl (PNL) is a carbon-centered neutral π -radical with a delocalized spin structure.^{12–19} Several PNL derivatives form π -dimers, and exhibit

absorption bands around 600 nm.^{15–17} In a few cases, 1D π -stacking columns are formed with large intermolecular separations of ~ 3.78 (ref. 13) and 3.65 Å,¹⁹ due to bulky protection groups, the latter of which shows a band around 800 nm.¹⁹ π -Stacked structures of π -conjugated PNL dimers (1/2 unpaired electron per PNL unit)^{20–22} and those of singlet-diradical bisphenalenyls²³ (one unpaired electron per PNL unit) exhibit NIR absorption bands. Bis(dithiazolyl) radicals^{24, 25} form 1D π -stacks with intercolumnar S...S and S...N contacts, showing low-energy absorption bands around ~ 2500 nm (~ 0.5 eV).

Trioxotriangulene (TOT) **1**, a neutral π -radical possessing a delocalized SOMO (Fig. 1), was designed by the π -expansion and oxo-substitution of PNL.²⁶ In this study, we found that TOT derivatives having *tert*-butyl and *n*-butoxy groups, **2** and **3**, respectively, exhibit a strong self-assembling ability to form 1D π -stacking columns. In the following section, NIR absorptions with wavelengths longer than 1000 nm for π -stacked radical polymers are reported. The mechanism of NIR absorption is elucidated using a quantum chemical calculation. Sufficiently long columns should be handled to obtain excitation energy compared to the absorption spectra of simple crystals. The quantum chemical calculation of such system is difficult due to the large scaling of computational time with respect to the size of systems. We focus on our linear-scaling method for nonlocal electronic excitations developed recently.²⁷ The use of the effective algorithm provides

¹Department of Chemistry and Biochemistry, School of Advanced Science and Engineering, Waseda University, Shinjuku 169-8555 Tokyo, Japan; ²Research Institute for Science and Engineering, Waseda University, Shinjuku 169-8555 Tokyo, Japan; ³CREST, Japan Science and Technology Agency, Kawaguchi 332-0012 Saitama, Japan; ⁴Department of Chemistry, Graduate School of Science, Osaka University, Toyonaka 560-0043 Osaka, Japan; ⁵The Institute for Solid State Physics, The University of Tokyo, Kashiwa 277-8581 Chiba, Japan; ⁶Department of Applied Chemistry, Faculty of Engineering, Aichi Institute of Technology, Toyota 470-0392 Aichi, Japan; ⁷Department of Advanced Materials Science, Graduate School of Frontier Sciences, The University of Tokyo, Kashiwa 277-8561 Chiba, Japan and ⁸Elements Strategy Initiative for Catalysts and Batteries (ESICB), Kyoto University, Nishikyo-ku 615-8245 Kyoto, Japan

Correspondence: Yasushi Morita (moritay@aitech.ac.jp) or Hiromi Nakai (nakai@waseda.jp)

Received: 7 January 2017 Revised: 9 May 2017 Accepted: 15 May 2017

Published online: 08 June 2017

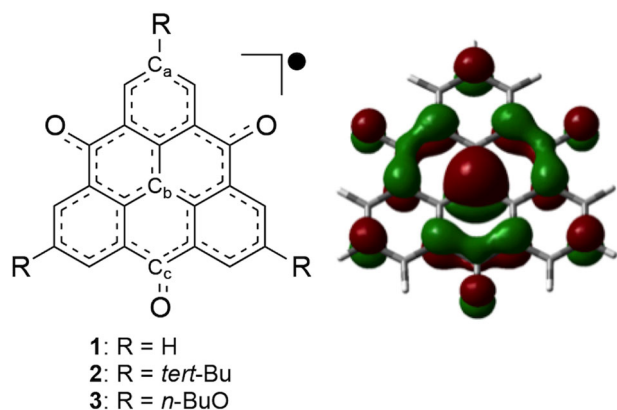


Fig. 1 Chemical structure and SOMO of TOT. **R** denotes the substituent groups around the TOT skeleton. The SOMO was obtained by restricted open-shell DFT using the ω B97X-D functional

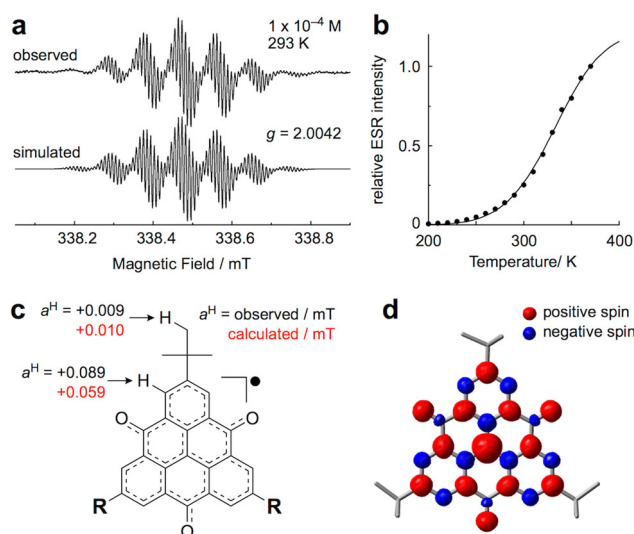


Fig. 2 Electronic spin structure of **2**. **a** Observed and simulated hyperfine electron paramagnetic resonance (EPR) spectra of **2** in toluene (1×10^{-4} M) at 293 K. **b** Temperature dependence of the EPR intensity of **2** in toluene (8×10^{-5} M), where *plot* and *solid line* denote the experimental values normalized at 370 K and the calculated value. **c** Observed (*black*) and calculated (*red*) hfcc values of **2**. **d** Calculated spin-density distribution of **2**. *Red* and *blue* regions denote positive and negative spin densities, respectively

a consistent explanation of the experimental spectra of single crystals on the basis of the properties of a monomer or a dimer.

RESULTS

Synthesis and spectroscopy

Neutral radicals **2** and **3** were synthesized according to our previous work²⁶ and Supplementary Fig. 1, respectively. Novel radical **3** is stable in air at room temperature in both the solid and solution states, indicating the high chemical stability of **3** similar to **2**,²⁶ despite its smaller steric hindrance. Such a high stability is originated from the delocalization of electronic spin around the extended π -electronic system (Fig. 2 and Supplementary Fig. 2). Figure 2a shows the observed and simulated electron paramagnetic resonance (EPR) spectra of **2** in toluene, showing a well-resolved multiline spectrum originating from the hyper-fine couplings with hydrogen atoms on aromatic ring and *tert*-butyl

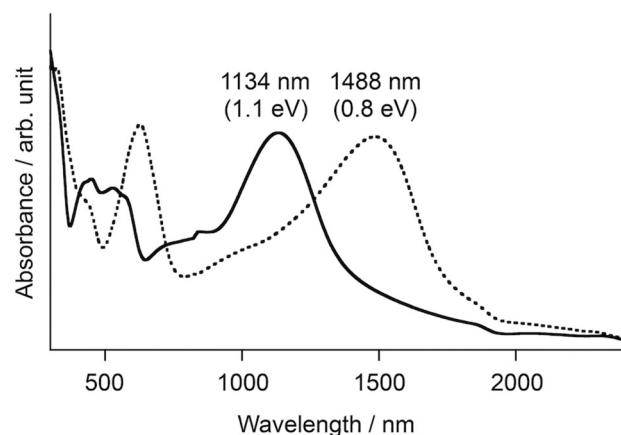


Fig. 3 Solid state absorption spectra. The *solid* and *dashed* lines show the spectra of **2** and **3**, respectively. Measurement was performed for the KBr pellets

groups. The hyper-fine coupling constants (a^H) determined by the simulation are successfully assigned with the help of the density functional theory (DFT) calculations (Fig. 2c), suggesting that the unpaired electron of **2** delocalizes over the whole π -electronic system with threefold symmetry as seen in the calculated spin-density map (Fig. 2d). The intensity of the EPR signal of **2** gradually decreased on cooling (Fig. 2b) due to the π -dimerization as shown in PNL radical (*vide infra*),^{16, 17} and the fitting of the plot gave the thermal parameters of π -dimerization,¹⁶ $\Delta H = -12.7(4)$ kcal mol⁻¹ and $\Delta S = -19(2)$ e.u.

Figure 3 displays solid-state absorption spectra of **2** and **3** dispersed in KBr. **2** shows a long-wavelength broad absorption band centered at 1134 nm. In the polarized reflectance spectra of a single crystal of **2** (Supplementary Figs. 3 and 4), this absorption was observed only along the column direction. A similar absorption band was also observed for **3** around 1488 nm in both KBr pellet and polarized reflectance spectra (Fig. 3 and Supplementary Fig. 4). These anisotropic absorption spectra clearly indicate that the long-wavelength absorptions of **2** and **3** are derived from intra-columnar π - π interactions in the solid state.

The solution spectrum of **2** in CHCl_3 shows a long-wavelength absorption band centered at 834 (Fig. 4), and similar band is observed for **3** at 978 nm (Supplementary Fig. 5). The time-dependent density functional theory (TDDFT) calculation assigned the band as the intermolecular transition within π -dimers,^{15–17} and the wavelengths are significantly shorter than that in the solid state, suggesting a stacking effect in the column. For the detailed assignment, excited-state calculations of monomers and π -dimers were performed (Supplementary Tables 1–3). In the temperature-dependent measurement, the bands assignable as the monomer (labeled as D in Fig. 4) becomes weak with lowering temperature, while the intensity of the band of the π -dimer (labeled as S in Fig. 4) increases on cooling. They are fully reversible and have isosbestic points, indicating that the spectral changes are due to thermal equilibrium between only two species, the monomer and π -dimer of **2** in a solution state. These experimental and calculation results eliminate the possibility of the generation of the σ -dimer in the solution state at low temperature. It should be also noted that the σ -dimerization cut the π -electronic systems of TOT skeleton into pieces, then the σ -dimer of **2** is hardly expected to exhibit a longer wavelength absorption. In the case of tri-*tert*-butyl-1,3-diazapNL radical,¹¹ where the π - and σ -dimers coexist in the equilibrium in the solid state, a long-wavelength absorption around 670 nm reduces with lowering temperature and increasing the ratio of the σ -dimer. Tri-*tert*-butyl PNL radical forms a π -dimer in the solution state at low temperature as well as in the crystalline

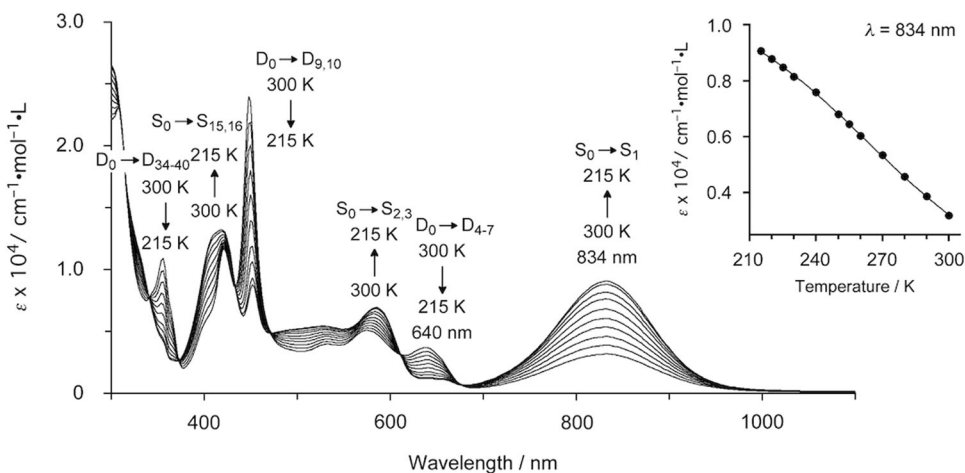


Fig. 4 Temperature-dependent UV-Vis spectra of **2** in CHCl_3 solution (8.25×10^{-5} M). Assignments by the TDDFT calculation of monomer (doublet, D) and dimer (singlet, S) were shown. *Inset* shows the plot of temperature dependence of the absorbance at 834 nm

state, and the π -dimer exhibits a long-wavelength absorption band around 600 nm.^{16, 17} Considering these previous studies of π -dimers of PNL-based π -radicals, the present long-wavelength broad absorption is assignable to a transition within the π -dimeric pair of **2**, namely, the radical **2** in solution aggregates to form the π -dimers.

Importantly, the broad absorption band of **2** centered at 834 nm increases with decreasing temperature as shown in the inset of Fig. 4. Solid line shows the calculated dependencies with the theoretical values with $\Delta H = -6.2(1)$ kcal mol⁻¹ and $\Delta S = -4.4(4)$ e. u. Although the reason is not clear, the differences of these ΔH and ΔS values from those obtained by the EPR measurement (Fig. 2) are probably caused by the solvent effect. In the case of the π -dimerization of tri-*tert*-butyl PNL radical,^{16, 17} the thermodynamic parameters considerably varied depending on the measurement solvents, indicating that the π -dimerization of π -radicals is very sensitive to solvation.

Crystal structure

Figure 5 describes 1D column structures of **2** (ref. 26) and **3** in the crystals, where both molecules stack by π - π interaction and σ -dimerization of the radicals is not observed. In both columns, the molecules stack to enclose the C_b atoms, which possesses the largest spin population (Fig. 5a, b). The shortest intermolecular C_b - C_b distances of **2** and **3** dimers are 2.979 and 3.084 Å, respectively, and those around 1.5 Å indicating σ -dimerization of the radicals are not observed. Two different distances between C_b atoms defined in Fig. 1: 2.979 and 3.641 Å for **2**, and 3.084 and 3.452 Å for **3**, suggest the π -dimerization in the columns (Fig. 5c, d). The intradimer C_b - C_b distances are much smaller than the sum of van der Waals radii of carbon atoms, 3.40 Å.²⁸ Some of the other intradimer C-C and C-O distances also show the same tendency. In contrast, interdimer C-C and C-O distances are longer than the sums of the van der Waals radii. The fact means that the 1D column structure is made of sequential stacking of π -dimers. The intra/interdimer overlap integrals between π -orbitals in the columns of **2** and **3** calculated by the extended Hückel method are $18.4/1.15 \times 10^{-3}$ and $-20.3/-11.4 \times 10^{-3}$, respectively, indicating stronger dimerization of **2** over that of **3**.

Quantum chemical calculation of π -stacked radical polymers

To understand the NIR absorption theoretically, finite column structures were extracted, and photoexcitation properties were determined by a quantum chemical calculation. First, the electron excitation from the ground (S_0) state to low-lying singlet states of

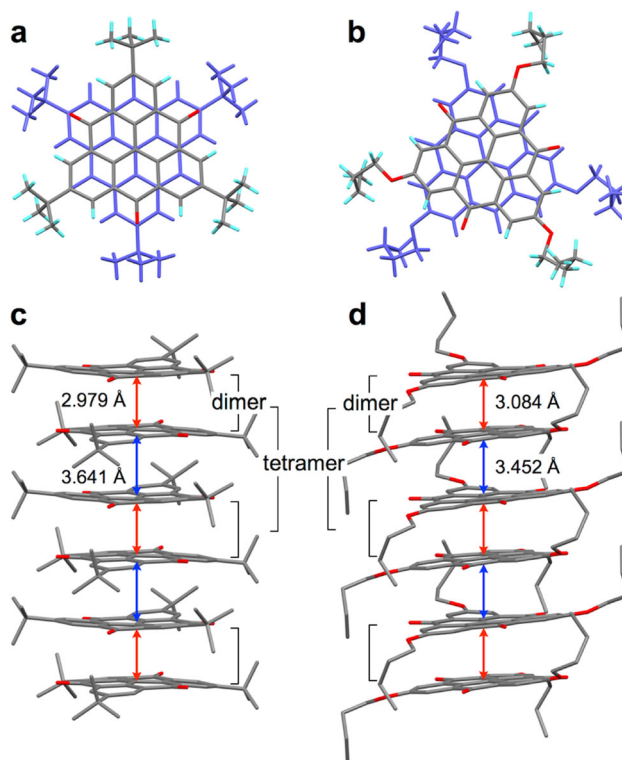


Fig. 5 Crystal structures of **2** and **3**. **a, b** Overlap patterns of **2** (ref. 26) and **3** in the 1D columns, respectively. **c, d** The column structures of **2** (ref. 26) and **3**, where red and blue arrows designate intradimer and interdimer distances between C_b atoms, respectively

dimers and tetramers of **2** and **3** were calculated (Table 1). Here a dimer and a tetramer are defined as shown in Fig. 5c, d. For the dimer, the $S_0 \rightarrow S_1$ transition has a large oscillator strength. This excitation corresponds to a HOMO-LUMO transition, where HOMO and LUMO are generated by a SOMO from each monomer (Fig. 6). The excitation character is the same as that of a π -stacked PNL dimer.¹⁵⁻¹⁷ In the tetramer, four SOMOs provide two bonding and two anti-bonding orbitals (Supplementary Fig. 6), generating four excited states. The lowest excitation has large oscillator strength and smaller excitation energy than the $S_0 \rightarrow S_1$ transition of the dimer. In contrast, the higher excitations have zero or

Table 1. Electronic excitation properties of dimers and tetramers of **2** and **3** by quantum chemical calculations

	Energy (eV)	Wavelength (nm)	Oscillator strength	Configuration	
Dimer of 2					
$S_0 \rightarrow S_1$	1.598	776	0.237	HOMO \rightarrow LUMO	0.716
Tetramer of 2					
$S_0 \rightarrow S_1$	1.440	861	0.599	HOMO - 1 \rightarrow LUMO + 1	-0.306
				HOMO \rightarrow LUMO	0.644
$S_0 \rightarrow S_2$	1.639	757	0.000	HOMO - 1 \rightarrow LUMO	0.544
				HOMO \rightarrow LUMO + 1	-0.467
$S_0 \rightarrow S_3$	2.129	582	0.000	HOMO - 1 \rightarrow LUMO	0.459
				HOMO \rightarrow LUMO + 1	0.537
$S_0 \rightarrow S_4$	2.242	553	0.004	HOMO - 1 \rightarrow LUMO + 1	0.639
				HOMO \rightarrow LUMO	0.302
Dimer of 3					
$S_0 \rightarrow S_1$	1.245	996	0.174	HOMO \rightarrow LUMO	0.721
Tetramer of 3					
$S_0 \rightarrow S_1$	1.097	1130	0.434	HOMO - 1 \rightarrow LUMO + 1	-0.298
				HOMO \rightarrow LUMO	0.651
$S_0 \rightarrow S_2$	1.286	964	0.000	HOMO - 1 \rightarrow LUMO	0.546
				HOMO \rightarrow LUMO + 1	-0.473
$S_0 \rightarrow S_3$	1.739	713	0.000	HOMO - 1 \rightarrow LUMO	0.458
				HOMO \rightarrow LUMO + 1	0.532
$S_0 \rightarrow S_4$	1.868	664	0.001	HOMO - 1 \rightarrow LUMO + 1	0.641
				HOMO \rightarrow LUMO	0.286

Only the excitations between frontier orbitals made from monomer's SOMOs were summarized. Dominant configurations with coefficients larger than 0.20 are listed

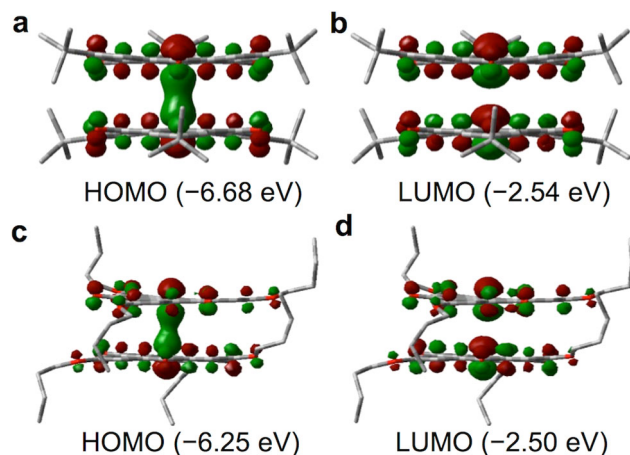


Fig. 6 Frontier orbitals and orbital energies of dimers of **a**, **b** **2** and **c**, **d** **3**. The HOMOs and LUMOs indicate intermolecular bonding and antibonding interactions due to the SOMOs of the monomers, respectively

negligibly small oscillator strengths and increased excitation energies.

Taking these results, the $S_0 \rightarrow S_1$ excitation energy, excitation wavelength, and HOMO-LUMO gap up to a 60mer were calculated. We calculated the systems from a dimer to a decamer using the conventional algorithm of TDDFT.²⁹ TDDFT calculations of the larger systems, i.e., 20–60 mers, were calculated using the divide-and-conquer Green function (DC-GF) method.²⁷ The DC-GF method reduces the scaling of computational cost to quasilinear. The dimension of the calculation was significantly decreased, as shown in Supplementary Table 4.

As seen in Table 2, the excitation energy decreases as the number of radicals, N , increases. The result of the 60 mers agrees well with the experimental absorption peak. The convergence of wavelength with respect to the number of radicals is confirmed. The oscillator strength was also calculated, up to a decamer (Table 2). The oscillator strength per molecule increases, indicating that the extension of the 1D structure enhances the photoabsorption. The configuration relevant to the $S_0 \rightarrow S_1$ excitation is qualitatively described in Fig. 7. In oligomers, the HOMO \rightarrow LUMO transition is the most dominant as in the dimer, while other configurations between frontier orbitals made from SOMOs such as HOMO - 1 \rightarrow LUMO + 1 and HOMO - 2 \rightarrow LUMO + 2 contribute to the electronic excitation.

Comparison between the calculated values of **2** and **3** in Table 2 indicates two tendencies: **3** has a longer absorption wavelength, and **2** has a larger oscillator strength. The larger intradimer orbital overlap of **2** leads to the wider HOMO-LUMO splitting of the oligomers. The larger oscillator strength of **2** than that of **3** is explained by the difference in excitation energy, because the oscillator strength is proportional to the energy difference between ground and excited states.

The substituent effect was also investigated by replacing the substituents with hydrogen (Supplementary Table 5). From the result of the 60 mers, red shifts due to the substituents were 67 and 119 nm for **2** and **3**, respectively. The rationale of this substituent effect is the delocalization of SOMOs into the substituents (Supplementary Fig. 7), resulting in smaller SOMO-SOMO overlap. The delocalization is consistent with the decrease in spin population at the C_b atom (Supplementary Table 6).

Here we discuss the reason of the longer absorption wavelength of **3** compared to **2** in the crystalline phase. The differences of the calculated excitation wavelengths between the dimers of **2** and **3** with and without substituents are 220 and 227 nm, respectively. Although **2** forms a staggered dimer, the dimer

of **3** is twisted at about 32° , decreasing the overlap of SOMOs, as calculated in the previous subsection. The smaller overlap narrows the HOMO-LUMO gap, decreasing the excitation energy. Non-covalent attractive interactions between *n*-butoxy side chains may elucidate the twisted structure. From the comparison between absorption wavelengths of dimers and 60 mers, the difference of the calculated excitation wavelengths for **2** and **3** increased by 225 nm (with substituents) and 166 nm (without substituents), respectively. Thus, the interdimer excitonic delocalization is also key to explain the difference of experimental absorption wavelengths of crystals (354 nm). Such large intermolecular effect

is reasonable because the interdimer atom-atom distances of **3** are smaller than those of **2**.

The column length dependence of the excitation wavelength obtained by quantum chemistry calculations is visualized in Fig. 8. The excitation wavelength has converged at the 60 mer, indicating that the 60 mer is sufficient to represent the photoabsorption of the infinitely long column. The substituent effect in increasing the excitation wavelength is not negligible. The excitation wavelength increases as the number of layers increases to the 30 mer, and the increase from the 30 mer is not more than 20 nm. Considering the intradimer and interdimer distances shown in Fig. 5c, d, the column lengths, defined here as the longest distance between the central carbon atoms C_b (Fig. 1), of the 30 mers of **2** and **3** are 9.93 and 9.80 nm, respectively. Thus, the excitonic interaction is regarded to exist in the range of the column length of about 10 nm.

<i>N</i>	Energy (eV)	Wavelength (nm)	Oscillator strength	HOMO-LUMO gap (eV)
2	2 1.598	776	0.237 (0.119)	4.136
	4 1.440	861	0.599 (0.150)	3.783
	6 1.349	919	0.986 (0.164)	3.621
	8 1.296	957	1.400 (0.175)	3.537
	10 1.262	983	1.828 (0.183)	3.487
	20 1.188	1044		3.436
	30 1.155	1073		3.424
	40 1.146	1082		3.418
	50 1.145	1083		3.417
	60 1.145	1083		3.417
3	2 1.245	996	0.174 (0.087)	3.750
	4 1.097	1130	0.434 (0.109)	3.376
	6 1.007	1231	0.717 (0.120)	3.201
	8 0.953	1301	1.023 (0.128)	3.106
	10 0.919	1349	1.343 (0.134)	3.049
	20 0.845	1468		2.986
	30 0.822	1508		2.973
	40 0.812	1526		2.967
	50 0.812	1527		2.967
	60 0.811	1528		2.967

Excitation energies, wavelengths, oscillator strengths, and HOMO-LUMO gaps of 1D stacked **2** and **3** were obtained by quantum chemical calculations. *N* is the number of molecules. Oscillator strengths per molecule are shown in parentheses

DISCUSSION

We have disclosed and theoretically analyzed the strong NIR absorption of TOT derivatives **2** and **3** in the crystalline state. In the present system, the high stability and the extended π -systems of **2** and **3** caused π -dimers, leading to the construction of π -stacked radical polymers and exhibition of strong NIR absorption bands. With the help of TDDFT calculations, the absorption was interpreted in terms of the intradimer HOMO-LUMO transition and interdimer interaction of the transition moments. The calculation reproduced well the peaks in the absorption spectra. Although the quantum chemical calculations on the optical properties of π -dimers are reported in PNL radicals and several ionic radical species,^{15, 30, 31} the calculation on π -stacked radical polymers has not been performed. For designing the functional materials based on organic π -radicals, the development of computational analyses on the assemblies of open-shell molecules is indispensable. The present study will be useful in the exploration of new functional electronic and optical materials composed of organic π -radicals.

METHODS

Experimental section

The experimental details are described in the [Supplementary Information](#). Crystal data for **3**: $C_{34}H_{33}O_6$; $M_r = 537.60$, orthorhombic, space group $P2_12_12_1$ (no. 19), $a = 6.5294(7)$, $b = 26.765(3)$, $c = 30.426(3)$ Å, $V = 5316.7(9)$ Å³, $\rho_{\text{calcd}} = 1.343$ g cm⁻³, $Z = 8$, $T = 100$ K, $\mu(\text{MoK}\alpha) = 0.91$ cm⁻¹, $2\theta_{\text{max}} = 55.0^\circ$, 52,924 reflections, 12,205 of which were unique ($R_{\text{int}} = 0.209$). $R_1 = 0.0896$, $wR_2 = 0.2571$, GOF = 0.925. CCDC-1059198 contains the supplementary crystallographic data for this paper. These data can be obtained

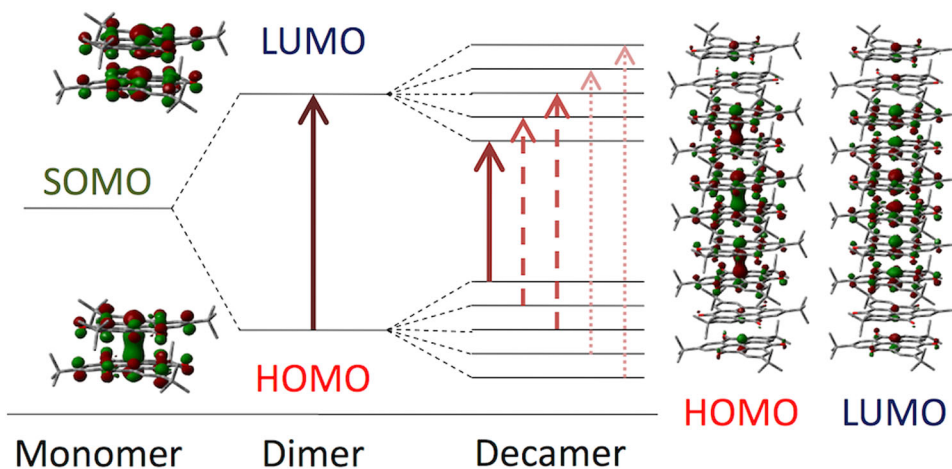


Fig. 7 Schematic illustration on $S_0 \rightarrow S_1$ excitation of a dimer and a decamer of **2**. Horizontal lines represent energy levels of frontier orbitals. HOMO and LUMO of a dimer and a decamer are depicted as well as SOMO of a monomer

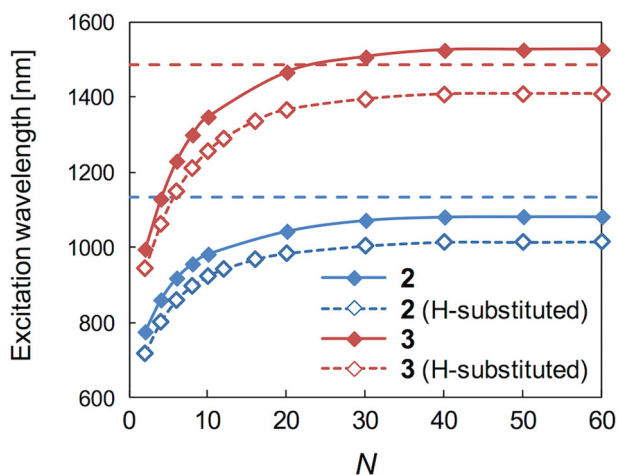


Fig. 8 Dependence of $S_0 \rightarrow S_1$ calculated excitation wavelength on the number of stacked radicals, N . *Blue and red broken lines* mean experimental peaks of photoabsorption spectra of single crystals **2** and **3**, respectively. The calculated data were taken from Table 2 (**2** and **3**) and Supplementary Table 5 (hydrogen-substituted **2** and **3**)

free of charge from The Cambridge Crystallographic Data Centre via www.ccdc.cam.ac.uk/data_request/cif.

Theoretical calculation

DFT and TDDFT calculations were carried out to compute ground and excited states, respectively. Here we mention our state-of-the-art algorithm for TDDFT, DC-GF method.²⁷ Computational details in the other calculations are summarized in the [Supplementary Information](#).

In usual TDDFT calculations to obtain excitation energies and properties, the so-called Casida's equation²⁹ is solved. The DC-GF method was proposed for large-scale excited-state calculations, where an exciton is significantly delocalized. Instead of solving the Casida's equation in conventional TDDFT, the DC-GF method evaluates excitation energies using frequency-dependent dynamical polarizabilities.

The dynamical polarizability of a system is expressed by two formulae. The first formula is a derivative of the total dipole moment with respect to the external electric field. This is equivalent to solving the Green function method.^{32, 33} The DC method for electronic structure calculation,^{34–36} which divides the total system into subsystems and allocates buffer region for each subsystem, reduced the scaling of computational time to quasilinear. The second formula is expressed as the sum-over-state, as follows:

$$\alpha(\omega) = \sum_n \frac{f_n}{\omega_n^2 - \omega^2}, \quad (1)$$

where ω_n and f_n are the excitation energy and oscillator strength from the ground state to the n -th excited state, respectively; n describes any excited state. At the pole corresponding to the n -th excited state, the dynamical polarizability is approximated as

$$\alpha(\omega) \approx \frac{f_n}{\omega_n^2 - \omega^2}. \quad (2)$$

When the polarizabilities of both ω_{n+} and ω_{n-} frequencies are sufficiently close to ω_n , the excitation energy, ω_n is calculated using

$$\omega_n = \sqrt{\frac{\alpha(\omega_+) \omega_+^2 - \alpha(\omega_-) \omega_-^2}{\alpha(\omega_+) - \alpha(\omega_-)}}. \quad (3)$$

The DC-GF method is equivalent to solving the Casida's equation in terms of providing the poles at the same frequencies. To determine the excitation energies close to an unknown pole, we have recently proposed an efficient pole-search algorithm,³⁷ which combines a homogeneous search using a constant energy step with a bisection search.

We applied the DC-GF method to 20–60 mers of **2** and **3** (Table 2) and 10–60 mers of hydrogen-substituted counterparts (Supplementary Table 5). A modified version of the GAMESS program³⁸ was used with the ω B97X-D³⁹ functional and 6–31 G(d,p) basis set. The spin-restricted formalism was

employed because spin density of **2** in solution disappeared at low temperature due to the formation of a dimer (Fig. 2b). One dimer and two tetramers were taken as a central and buffer regions of the DC method, respectively. The number of singly excited configurations is listed in Supplementary Table 4. The maximum size of the system treated by the DC-GF method is the 60 mer of **3**, containing 4380 atoms and 45,900 basis functions. If the conventional algorithm is applied, 229,702,500 singly excited configurations should be treated. The maximum number of singly excited configurations per subsystem in the DC-GF method was 6,380,625. The reduction of computational cost realized large-scale TDDFT calculations to support the interpretation of the NIR absorption.

The data that support the findings of this study are available from the corresponding author on reasonable request.

ACKNOWLEDGEMENTS

We thank Prof. Takeji Takui and Prof. Kazunobu Sato in Osaka City University for their technical assistance and fruitful discussions on the ESR measurements. NIR reflectance spectra were measured at BL43IR beam line of SPring-8 (proposal No. 2015B1133), and we appreciate Dr Yuka Ikemoto in Japan Synchrotron Radiation Research Institute (JASRI) for the technical support. Some of the present calculations were performed at the Research Center for Computational Science (RCCS), Okazaki Research Facilities, and National Institutes of Natural Sciences (NINS). We thank the Core Research for Evolutional Science and Technology (CREST) Program 'Creation of Innovative Functions of Intelligent Materials on the Basis of the Element Strategy' of the Japan Science and Technology Agency (JST).

AUTHOR CONTRIBUTIONS

Y.I., Q.W., T.Y., and H.N. performed quantum chemical calculations of **1**, **2**, and **3**. A.U., T.M., K.K., M.M., and Y.M. synthesized and measured physical properties of **2** and **3**. H. O. measured polarized reflectance spectra of **2**. All authors wrote and reviewed the manuscript.

ADDITIONAL INFORMATION

Supplementary Information accompanies the paper on the *npj Quantum Materials* website (doi:10.1038/s41535-017-0033-8).

Competing interests: The authors declare that they have no competing financial interests.

Publisher's note: Springer Nature remains neutral with regard to jurisdictional claims in published maps and institutional affiliations.

REFERENCES

- Qian, G. & Wang, Z. Y. Near-infrared organic compounds and emerging applications. *Chem. Asian J.* **5**, 1006–1029 (2010).
- Sun, Z., Ye, Q., Chi, C. & Wu, J. Low band gap polycyclic hydrocarbons: from closed-shell near infrared dyes and semiconductors to open-shell radicals. *Chem. Soc. Rev.* **41**, 7857–7889 (2012).
- Tsuda, A. & Osuka, A. Fully conjugated porphyrin tapes with electronic absorption bands that reach into infrared. *Science* **293**, 79–82 (2001).
- Mori, H., Tanaka, T. & Osuka, A. Fused porphyrinoids as promising near-infrared absorbing dyes. *J. Mater. Chem. C* **1**, 2500–2519 (2013).
- Simpson, C. D. et al. Synthesis of a giant 222 carbon graphite sheet. *Chem. Eur. J.* **8**, 1424–1429 (2002).
- Hiramoto, M., Kitada, K., Iketani, K. & Kaji, T. Near infrared light driven organic *p-i-n* solar cells incorporating phthalocyanine *J*-aggregate. *Appl. Phys. Lett.* **98**, 023302 (2011).
- Torrance, J. B., Scott, B. A., Welber, B., Kaufman, F. B. & Seiden, P. E. Optical properties of the radical cation tetrathiafulvalenium (TTF⁺) in its mixed-valence and monovalence halide salts. *Phys. Rev. B* **19**, 730–741 (1979).
- Torrance, J. B. The difference between metallic and insulating salts of tetracyanoquinodimethone (TCNQ): how to design an organic metal. *Acc. Chem. Res.* **12**, 79–86 (1979).
- Yamaguchi, S., Moritomo, Y. & Tokura, Y. Pressure effect on the optical gap transition in a Peierls-Hubbard system: potassium-tetracyanoquinodimethane. *Phys. Rev. B* **48**, 6654–6657 (1993).
- Meneghetti, M. Optical properties of one-dimensional π -conjugated compounds: study of the pressure-dependent linear properties of K-tetracyanoquinodimethane. *Phys. Rev. B* **50**, 16899–16904 (1994).
- Morita, Y., Suzuki, S., Sato, K. & Takui, T. Synthetic organic spin chemistry for structurally well-defined open-shell graphene fragments. *Nat. Chem.* **3**, 197–204 (2011).

12. Goto, K. et al. A stable neutral hydrocarbon radical: synthesis, crystal structure, and physical properties of 2,5,8-Tri-*tert*-butyl-phenalenyl. *J. Am. Chem. Soc.* **121**, 1619–1620 (1999).
13. Koutentis, P. A. et al. Perchlorophenalenyl radical. *J. Am. Chem. Soc.* **123**, 3864–3871 (2001).
14. Morita, Y. & Nishida, S. Phenalenyls, cyclopentadienyls, and other carbon-centered radicals. in *Stable Radicals: Fundamental and Applied Aspects of Odd-Electron Compounds* (ed. Robin G. Hicks) 81–145 (Wiley, 2010).
15. Lü, J.-M., Rosokha, S. V. & Kochi, J. K. Stable (long-bonded) dimers via the quantitative self-association of different cationic, anionic, and uncharged π -radicals: structures, energetics, and optical transitions. *J. Am. Chem. Soc.* **125**, 12161–12171 (2003).
16. Small, D. et al. Intermolecular π -to- π bonding between stacked aromatic dyads. experimental and theoretical binding energies and near-IR optical transitions for phenalenyl radical/radical versus radical/cation dimerizations. *J. Am. Chem. Soc.* **126**, 13850–13858 (2004).
17. Suzuki, S. et al. Aromaticity on the pancake-bonded dimer of neutral phenalenyl radical as studied by MS and NMR spectroscopies and NICS analysis. *J. Am. Chem. Soc.* **128**, 2530–2531 (2006).
18. Mou, Z., Uchida, K., Kubo, T. & Kertesz, M. Evidence of σ - and π -dimerization in a series of phenalenyls. *J. Am. Chem. Soc.* **136**, 18009–18022 (2014).
19. Uchida, K. et al. Dual association modes of the 2,5,8-tris(pentafluorophenyl) phenalenyl radical. *Chem. Asian J.* **9**, 1823–1829 (2014).
20. Itkis, M. E., Chi, X., Cordes, A. W. & Haddon, R. C. Magneto-opto-electronic bistability in a phenalenyl-based neutral radical. *Science* **296**, 1443–1445 (2002).
21. Pal, S. K. et al. Resonating valence-bond ground state in a phenalenyl-based neutral radical conductor. *Science* **309**, 281–284 (2005).
22. Kubo, T. et al. Synthesis, crystal structure, and physical properties of sterically unprotected hydrocarbon radicals. *J. Am. Chem. Soc.* **133**, 14240–14243 (2011).
23. Shimizu, A. et al. Resonance balance shift in stacks of delocalized singlet biradicals. *Angew. Chem. Int. Ed.* **121**, 5590–5594 (2009).
24. Beer, L. et al. Prototypal dithiazolodithiazolyl radicals: synthesis, structures, and transport properties. *J. Am. Chem. Soc.* **125**, 14394–14403 (2003).
25. Leitch, A. A. et al. An alternating π -stacked bisdithiazolyl radical conductor. *J. Am. Chem. Soc.* **129**, 7903–7914 (2007).
26. Morita, Y. et al. Organic tailored batteries materials using stable open-shell molecules with degenerate frontier orbitals. *Nat. Mater.* **10**, 947–951 (2011).
27. Nakai, H. & Yoshikawa, T. Development of an excited-state calculation method for large systems using dynamical polarizability: a divide-and-conquer approach at the time-dependent density functional level. *J. Chem. Phys.* **146**, 124123 (2017).
28. Bondi, A. van der Waals volumes and radii. *J. Phys. Chem.* **68**, 441–451 (1964).
29. Casida, M. E. Time-dependent density functional response theory for molecules. in *Recent Advances in Density Functional Methods*, Vol. 1 (ed. Delano P. Chong) **1**, 155–192 (World Scientific, Singapore, 1995).
30. Zhong, R.-L. et al. Boron/nitrogen substitution of the central carbon atoms of the biphenalenyl diradical π dimer: a novel 2e–12c bond and large NLO responses. *Chem. Eur. J.* **17**, 11773–11779 (2011).
31. Yoneda, K. et al. Third-order nonlinear optical properties of one-dimensional open-shell molecular aggregates composed of phenalenyl radicals. *Chem. Eur. J.* **20**, 11129–11136 (2014).
32. Ferrell, R. A. Time-dependent hartree-fock theory of nuclear collective oscillations. *Phys. Rev.* **107**, 1631–1634 (1957).
33. Thouless, D. J. Vibrational states of nuclei in the random phase approximation. *Nucl. Phys.* **22**, 78–95 (1961).
34. Yang, W. Direct calculation of electron density in density-functional theory. *Phys. Rev. Lett.* **66**, 1438–1441 (1991).
35. Akama, T., Kobayashi, M. & Nakai, H. Implementation of divide-and-conquer method including Hartree-Fock exchange interaction. *J. Comput. Chem.* **28**, 2003–2012 (2007).
36. Kobayashi, M., Imamura, Y. & Nakai, H. Alternative linear-scaling methodology for the second-order Møller-Plesset perturbation calculation based on the divide-and-conquer method. *J. Chem. Phys.* **127**, 074103 (2007).
37. Nakai, H., Yoshikawa, T. & Nonaka, Y. Efficient pole-search algorithm for dynamic polarizability: towards alternative excited-state calculation for large systems. *J. Comput. Chem.* **38**, 7–14 (2017).
38. Schmidt, M. W. et al. General atomic and molecular electronic structure system. *J. Comput. Chem.* **14**, 1347–1363 (1993).
39. Chai, J.-D. & Head-Gordon, M. Long-range corrected hybrid density functionals with damped atom-atom dispersion corrections. *Phys. Chem. Chem. Phys.* **10**, 6615–6620 (2008).



Open Access This article is licensed under a Creative Commons Attribution 4.0 International License, which permits use, sharing, adaptation, distribution and reproduction in any medium or format, as long as you give appropriate credit to the original author(s) and the source, provide a link to the Creative Commons license, and indicate if changes were made. The images or other third party material in this article are included in the article's Creative Commons license, unless indicated otherwise in a credit line to the material. If material is not included in the article's Creative Commons license and your intended use is not permitted by statutory regulation or exceeds the permitted use, you will need to obtain permission directly from the copyright holder. To view a copy of this license, visit <http://creativecommons.org/licenses/by/4.0/>.

© The Author(s) 2017